Microstructure-based Numerical Simulation of the Mechanical Behaviour of Ocular Tissue

Dong Zhou[1*], Ahmed Abass[1], Ashkan Eliasy[1], Harald P Studer[2], Alexander Movchan[3], Natalia Movchan[3], Ahmed Elsheikh[1, 4, 5]

[1]*School of Engineering, University of Liverpool*

[2]*Optimo Medical AG, Bienne, Switzerland*

[3]*Department of Mathematical Sciences, University of Liverpool*

[4]*NIHR Biomedical Research Centre for Ophthalmology, Moorfields Eye Hospital NHS Foundation Trust and UCL Institute of Ophthalmology, UK*

[5] *School of Biological Science and Biomedical Engineering, Beihang University, Beijing, China*

***Corresponding author:**

Zhou, Dong

School of Engineering, University of Liverpool, Liverpool L69 3GH, UK

sgdzhou3@liverpool.ac.uk

Keywords: cornea; sclera; microstructure of ocular tissue; numerical modelling; ocular biomechanics

Word count: 7005

Abstract

This paper aims to present a novel full-eye biomechanical material model that incorporates the characteristics of ocular tissues at microstructural level, and use the model to analyse the age-related stiffening in tissue behaviour. The collagen content in ocular tissues, as obtained using X-ray scattering measurements, was represented by sets of Zernike polynomials that covered both the cornea and sclera, then used to reconstruct maps of collagen fibril magnitude and orientation on the 3D geometry of the eye globe. Fine-mesh finite element (FE) models with eye-specific geometry were built and supported by a user-defined material model (UMAT), which considered the regional variation of fibril density and orientation. The models were then used, in an iterative inverse modelling study to derive the material parameters that represent the experimental behaviour of ocular tissues from donors aged between 50 and 90 years obtained in earlier ex-vivo studies. Sensitivity analysis showed that reducing the number of directions that represented the anisotropy of collagen fibril orientation at each X-ray scattering measurement point from 180 to 16 would have limited and insignificant effect on the FE solution (0.08%). Inverse analysis resulted in material parameters that provided a close match with experimental intraocular pressure-deformation behaviour with a root mean square (RMS) of error between 3.6% and 4.3%. The results also demonstrated a steady increase in mechanical stiffness in all ocular regions with age. A constitutive material model based on distributions of collagen fibril density and orientation has been developed to enable the accurate representation of the biomechanical behaviour of ocular tissues. The model offers a high level of control of stiffness and anisotropy across ocular globe, and therefore has the potential for use in planning surgical and medical procedures.

Introduction

Ocular numerical models have been widely used in a variety of biomechanical applications including medical device development and disease management (Salimi et al., 2011, Gefen et al., 2009, Elsheikh et al., 2009, Anderson et al., 2004, Sigal et al., 2004). Computer based simulations also have several advantages over laboratory experiments such as much reduced cost and more rapid evaluation. However, the effectiveness of numerical models relies on their ability to accurately represent the eye's geometry, loading, boundary conditions and biomechanical properties, the last of which is usually the most demanding feature in terms of characterisation and embedding in numerical models (Coudrillier et al., 2015, Whitford et al., 2015, Elsheikh et al., 2009, Anderson et al., 2004, Nejad et al., 2014).

Both the cornea and the sclera have complex material behaviour that is hyperelastic, viscoelastic, dependent on age and medical history and has significant regional variation of stiffness (Elsheikh et al., 2010b, Geraghty et al., 2012, Kling and Hafezi, 2017, Wolffsohn et al., 2012, Elsheikh et al., 2008a). In addition, the tissue of ocular globe is known to retain a high degree of anisotropy as its mechanical behaviour is dependent on the distribution of collagen fibrils, the main load carrying components of the tissue (Elsheikh et al., 2008b). With collagen fibrils showing significant regional variations in density and orientation, the biomechanical behaviour of the tissue changes accordingly, exhibiting stiffness levels that vary with location and direction, and making ocular biomechanics highly complex (Aghamohammadzadeh et al., 2004, Meek and Boote, 2009).

Computational finite element (FE) models of corneal tissue have been developed over the last decades especially in terms of material representation. At an early stage, linear elastic and homogenous material models were employed (Vito et al., 1989, Hanna et al., 1988), but later anisotropy and nonlinearity were introduced (Pandolfi and Holzapfel, 2008, Pandolfi and Manganiello, 2006, Whitford et al., 2015, Grytz and Meschke, 2009, McDonnell, 1996, Girard et al., 2009, Coudrillier et al., 2015, Studer et al., 2010). More recently, constitutive models that accounted for the nonlinear, viscoelastic and anisotropic material behaviour through consideration of fibril arrangements in the cornea and laboratory experiments of tissue mechanical performance have been developed (Whitford et al., 2017). These developments

have made corneal numerical models increasingly reliable through more accurate representation of material behaviour.

The present study aimed to take important steps towards the goal of multiscale modelling of the full eye globe, in which the regional variations of both stiffness and anisotropy were derived from reliable microstructure data. While earlier studies have relied on idealisations of microstructure data that assumed mainly orthogonal and circumferential fibril orientations in the central cornea and limbus, the purpose of this study was to directly link the modelling process to raw X-ray scattering data in an effective way that took into account the realistic regional variation in collagen fibril density and arrangement of fibrils (Whitford et al., 2015, Whitford et al., 2017, Pinsky et al., 2005, Studer et al., 2010). Further, the study aimed to extend microstructure-based models beyond the cornea to cover the full eye globe. This step is now possible with the availability of fibril arrangement data across the whole globe that has been reported in an earlier study (Pijanka et al., 2013).

Methods

Constitutive material model

The material model adopted in this study followed phenomenological formulation that fitted the microstructure data on collagen fibril distribution reported earlier (Studer et al., 2010). A strain energy function, representing nonlinear, anisotropic, and incompressible material behaviour, was defined by means of additive terms for non-collagen material or tissue matrix (Ψ_m), collagen fibrils (Ψ_A) and incompressibility or volume dilation Ψ_U:

$$\Psi = \overline{\Psi}_m(\bar{\mathbf{F}}) + \overline{\Psi}_A(\bar{\mathbf{F}}, \mathbf{a_0}, \mathbf{b_0}) + \Psi_U(J) \quad (1)$$

where $\mathbf{F}$ is the deformation gradient at any material point with a decoupled form of $\bar{\mathbf{F}} = J^{-1/3}\mathbf{IF}$, $\mathbf{I}$ is an identity tensor, $\mathbf{a_0}$ and $\mathbf{b_0}$ are the vectors defining the orientations of fibrils as tangential and out of tangential to the ocular surface, and J is the determinant of deformation gradient $\mathbf{F}$. $\Psi_U(J)$ was introduced to control the volume dilation (compressibility):

$$\Psi_U(J) = \frac{1}{D}(J-1)^2 \quad (2)$$

where D is a material constant that must have a small value (10^{-5}) to preserve the material incompressibility (Studer et al., 2010).

The combination of the decoupled $\overline{\Psi}_m$ and $\overline{\Psi}_A$ aimed to ensure that both ground substance matrix and collagen fibrils were contributing to the volume-distortional strain energy density. Following a study by Studer et al. (2010), the Neo-Hookean law was chosen for this application because of its ability to represent the hyperelasticity of ocular tissue and account for isotropic non-collagen material behaviour ($\overline{\Psi}_m$):

$$\overline{\Psi}_m(\bar{\mathbf{F}}) = C_{10}\left(\overline{I}_1 - 3\right) \tag{3}$$

where C_{10} is a material constant; $\overline{I_1} = tr(\bar{\mathbf{C}})$ is the first strain invariant after energy isochoric split of the volume contribution, and the decoupled form of Right Cauchy deformation gradient $\bar{\mathbf{C}} = \bar{\mathbf{F}}^{\mathbf{T}}\bar{\mathbf{F}}$.

The anisotropy term $\overline{\Psi}_A$ was modelled by considering two families of fibrils; the in-lamella fibrils ($\overline{\Psi}_{A,,Lam}$) and the inter-lamellae fibrils which create interactions between adjacent lamellae ($\overline{\Psi}_{A,Int}$). Regarding the second fibril family, an out-of-plane angle of $15°$ was used following earlier studies (Whitford et al., 2015, Studer et al., 2010). In addition, a weighted average function $\mathrm{K}(r, \varphi, \alpha, \theta_i)$ was employed to describe fibril distribution over 180 degrees at a general point and to allow the inclusion of both fibril families:

$$\overline{\Psi}_A(\bar{\mathbf{F}}, \mathbf{a_0}, \mathbf{b_0}) = \frac{1}{N}\sum_{i=0}^{N} \mathrm{K}(r, \varphi, \alpha, \theta_i)\left(\overline{\Psi}_{A,Lam}\left(\overline{I}_4\right) + \overline{\Psi}_{A,Int}(\overline{I}_6)\right) \tag{4}$$

Equation (4) did not apply the probability density function (Whitford et al., 2015, Studer et al., 2010) as the fibril density represented by $\mathrm{K}(r, \varphi, \alpha, \theta_i)$ in this study was given by Zernike polynomials where (r, φ, α) define the spherical coordinates at any point in a global coordinate system, while θ_i is the azimuthal angle that controls fibril orientation in a local coordinate system, Figure 1. The fourth and sixth invariants $\overline{I}_4, \overline{I}_6$ represent stretches in specific fibril directions where $\overline{I}_4$ = $\mathbf{a_0}\overline{\mathbf{C}}\mathbf{a_0}$ and $\overline{I}_6$ = $\mathbf{b_0}\overline{\mathbf{C}}\mathbf{b_0}$. Total anisotropic strain energy was

calculated as the sum of the contribution of all discretised fibrils at N orientations. These orientations numbered from 1 to N had the equal spacing over the continuous $180°$ from the local axis of $\mathbf{e_1}$ that was defined in the meridional tangent direction. Therefore, the discretised fibril orientations specified by θ_i were decided in the established local coordinate system once a reasonable number of orientations N was suggested. $\mathrm{K}(r, \varphi, \alpha, \theta_i)$ at one orientation specified by θ_i can form a density field function across all the spatial points with coordinates (r, φ, α). In order to select a representative value for N, a parametric study was performed and considered values between 3 and 180 where the effect of this variation was determined by assessing the apical displacement and reaching compromise between accuracy of model prediction and computational cost. Apical displacement was chosen in this parametric study as a result of the combined effects of both the cornea and sclera in the current eye model where the equator was prevented from movement in the Z direction. The results indicated that both accuracy and computational cost increase with higher values of N.

Further, the specific forms of $\overline{\Psi}_{A,Lam}$ and $\overline{\Psi}_{A,Int}$ (Equation 4) were defined by Markert et al. (2005) as:

$$\begin{aligned} \overline{\Psi}_{A,Lam}(\bar{I}_4) &= \frac{\mu_1}{\gamma_1}\left(\bar{I}_4^{\frac{\gamma_1}{2}} - 1\right) - \mu_1 ln\bar{I}_4^{\frac{1}{2}} \\ \overline{\Psi}_{A,Int}(\bar{I}_6) &= \frac{\mu_2}{\gamma_2}\left(\bar{I}_6^{\frac{\gamma_2}{2}} - 1\right) - \mu_2 ln\bar{I}_6^{\frac{1}{2}} \end{aligned} \tag{5}$$

where μ_1, γ_1 and μ_2, γ_2 are the material parameters for the two families of in-plane $\overline{\Psi}_{A,Lam}(\bar{I}_4)$ and out-of-plane $\overline{\Psi}_{A,Int}(\bar{I}_6)$ fibrils. Parameters μ controlled the initial stiffness of collagen fibrils and γ controlled the nonlinearity in the stress-strain material behaviour (Whitford et al., 2015). As the strain energy parameters, $\overline{\Psi}_{A,Lam}$ and $\overline{\Psi}_{A,Int}$ existed only when the fibrils were subjected to tension, i.e. when stretch parameters $\bar{I}_4$ and $\bar{I}_6$ were larger than 1, the crimping state of the fibrils was not considered. It was expected that the fibrils would cease contributing to the tissue's mechanical action once subjected to compression.

Fitting of fibril distribution

Wide-angle X-ray scattering technique (WAXS) has been used to investigate the eye tissue in this study (Meek & Boote, 2009). Experiments have been carried out at the IO2 unit of the UK's national synchrotron facility Diamond Light Source (Oxfordshire, UK) where a 40 µm width by 20 µm height micro-focus beam with λ=0.979 Å wavelength and 0.5 s exposure time was used. A vacuum-compatible Pilatus detector sensor has been placed at 350 mm behind the specimen to collect the X-ray reflections and a lead beam stop was located between the specimen and the detector to prevent any diffracted beam from damaging the detector's sensitive area.

A collagen fibril map of a healthy right eye without surgical or pathological history belonging to a 69-year-old donor was obtained and detailed in a previous study (Pijanka et al., 2013). The tissue of the ocular globe was scanned using X-ray scattering facility at Station I02, Diamond Light Source Synchrotron (Oxford, UK). For each scanned point, the fibril content in each of equally spaced 360 orientations covering 360° was measured. A challenge is caused by the mismatch between the locations of the X-ray scanned points and the locations of the finite element integration points, at which the fibril density microstructure data is required for the numerical models. This mismatch was addressed by fitting the microstructure X-ray data to surface polynomials that can then be used to estimate corresponding data at the integration points. The fibril density at an X-ray scanned point was discretised into N values in the N orientations considered based on the specific local coordinate system with a meridional axis $\mathbf{e_1}$, and angles $\theta_i (i = 1 : N)$ representing the fibril orientations. The fibril densities in each orientation θ_i and in different scanning points were treated as the Z (height) values in polynomials, while the locations of scanning points provided the X and Y coordinates. Zernike, Gaussian-Hermite and Orthogonal Fourier-Mellin polynomials were investigated with orders ranging between 5 and 25, and this step led to the use of Zernike polynomials as they provided the lowest fitting error on the collagen density across the full eye. The RMS of fit errors were 28.6%, 20.1% and 16.5% with Zernike orders 5, 15 and 25, respectively, while corresponding RMS errors (when the same number of polynomials were used) with Gaussian-Hermite were 30.8%, 25.4% and 23.3%, and with Orthogonal Fourier-Mellin were 27.7%, 21.4% and 18.5%, respectively.

Further, in order to maintain the main features of fibril distribution and keep to a minimum the difference between measured data and the data provided by the Zernike polynomials, the fitting process was conducted separately for 4 ocular zones; the central cornea, the limbus, the anterior and equatorial sclera, and the posterior sclera. An overlap area with width of 2.4 mm was allowed between each two adjacent zones to ensure smooth transition of data from one zone to the next, and this process was repeated for each fibril orientation angle. The values of Zernike polynomial coefficients were calculated using the least squares minimisation method (BjÓrck, 1996) for each of the four ocular zones considered (see the Supplementary Material). The least squares method was adopted in this analysis as it has been used successfully in the past in similar applications (Carvalho, 2005) and for its low computational cost; 5 seconds to calculate order 25 Zernike coefficients using a PC with Intel Core I7-4790 and 16GB RAM.

A study was conducted with Zernike orders between 5 and 25 to select a reasonable order that increased the fitting accuracy but avoided overfitting. In this study, the ten-fold cross-validation method was adopted in the overfitting analysis by dividing the total data set in each ocular zone and in each orientation into ten subsets with approximately equal sizes (Kohavi, 1995, Geisser, 2017). For each data subset, the mean prediction error was calculated while adopting the coefficients of Zernike polynomials calculated based on the other nine data subsets and while considering Zernike orders between 5 and 25. After repeating this process for all 10 data subsets, the order of Zernike polynomials that provided the most accurate data predictions (and hence least prediction errors) was determined for all fibril orientations and all ocular zones. And once the order of Zernike polynomials was determined, all the measured data was used in a final exercise to determine values of the polynomial coefficients (using the least squares method), which were then used to estimate the fibril content in each fibril orientation and each integration point.

This process was preceded by converting the XYZ coordinates of integration points into polar coordinates (R_n,φ), Figure 1, to be compatible with the polar basis of Zernike polynomials. The term R_n was normalised by α/α_l to the range 0 to 1 for the cornea and normalised by

$1 + (\alpha - \alpha_l)/(\pi - \alpha_l)$ to the range 1 to 2 for the sclera where α_l was the complementary angle α of the elevation angle of the limbus.

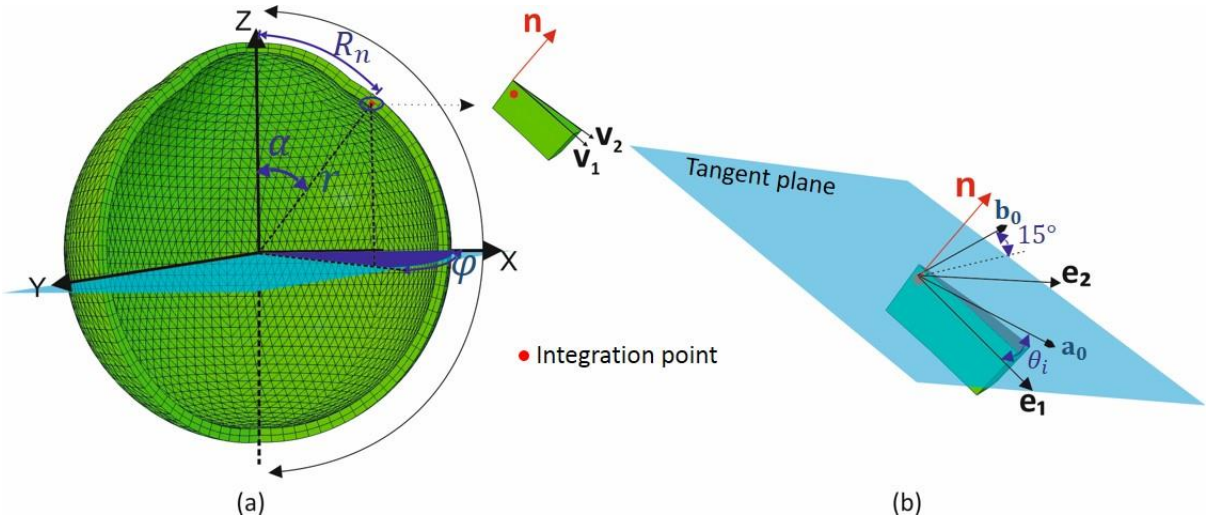

Figure 1 A schematic representation of fibril recruitment. (a) The global coordinate system was defined by (X, Y, Z), a general integration point was located by the spherical coordinates (r, α, φ), the normal vector was calculated by two vectors $\boldsymbol{v_1}$ and $\boldsymbol{v_2}$ for each element. (b) Two orthogonal vectors are located on the tangent plane with the unit vector $\boldsymbol{e_1}$ aligned in the meridional tangent direction. The two-unit vectors $\boldsymbol{e_1}, \boldsymbol{e_2}$ form the local coordinate system together with the normal vector $\boldsymbol{n}$. The in-plane fibril family, represented by $\boldsymbol{a_0}$, has the discretised orientation defined by azimuthal angle θ_i. The out-of-plane fibril family, represented by $\boldsymbol{b_0}$, has an orientation defined by θ_i and an out-of-plane rotation angle $15°$.

Implementation of constitutive model in numerical simulation

A constitutive model was implemented in numerical simulation using Abaqus 6.14 standard solver® (Dassault Systemes Simulia Crop., Rhode Island, USA) where two user subroutines (SDVINI and UMAT) were used to locate the model integration points, apply Zernike parameters and calculate stress and elasticity tensors that incorporate distribution of fibril content. Stress and elasticity tensors were derived based on the second Piola-Kirchhoff stress in the form (Weiss et al., 1996):

$$\mathbf{S} = 2\frac{\partial \Psi}{\partial \mathbf{C}} = 2\sum_{\mathrm{i}=1}^{6} \frac{\partial \Psi}{\partial I_i}\frac{\partial I_i}{\partial \mathbf{C}}$$
$$\mathbf{E} = 4\frac{\partial^2 \Psi}{\partial \mathbf{C}\,\partial \mathbf{C}} = 2\sum_{\mathrm{i}=1}^{6} \frac{\partial \mathbf{S}}{\partial I_i}\frac{\partial I_i}{\partial \mathbf{C}} \quad (6)$$

Subroutine SDVINI was programmed such that the pre-determined Zernike coefficients were used to estimate the fibril density at each integration point for each of the N orientations at the start of FE modelling analysis. The other subroutine, UMAT, was used to define a specific material model to control material behaviour by calculating the spatial version of elasticity tensor during each increment in loading. The fibril information calculated in SDVINI were passed to UMAT as location-based properties for each integration point.

Mesh density analysis

As mesh density can affect the convergence rate and accuracy of numerical models, a full eye model, whose geometry parameters were chosen based on earlier studies, was generated and used in a mesh density study, Figure 2a. The study included 10 models with a number of corneal elements between 432 and 2700, and a number of scleral elements between 6504 and 43764. All elements were 15-noded, solid, hybrid, and with quadratic formulation (C3D15H). The convergence was assessed by comparing the apical displacement and equator's radial expansion under 20 mmHg of intraocular pressure (IOP), which lies at the high end of the normal range of IOP; between 12 to 21 mmHg (Rezaie et al., 2002).

The material parameters adopted in this analysis were derived for ocular tissue with age 50 years (Whitford et al., 2015). Boundary conditions were set in a way, in which the equatorial nodes were restrained in the Z direction, while the corneal apex and posterior pole nodes were restrained in both the X and Y directions.

Inverse Analysis

Fibril densities were measured in arbitrary units and used initially as figures indicating the regional variation of stiffness across the ocular globe. The stiffness variation map was then calibrated (by determining values of the material parameters used in the strain energy model) through matching the numerical predictions of deformation under IOP with earlier experimental results. This matching was achieved through an inverse analysis process that was conducted to determine values of the six constitutive model parameters, D, C_{10}, μ_1, γ_1, μ_2 and γ_2, that were compatible with the material behaviour as determined experimentally in previous studies for ocular tissue aged between 50 and 90 years and subjected to IOP up to 30 mmHg (Geraghty et al., 2012, Elsheikh et al., 2010b). The experimental pressure-deformation behaviour obtained at 44 surface points on the ocular surface, and uniformly distributed on six meridians, Figure 2b, acted as the target behaviour in the inverse analysis process.

The inverse analysis included an optimisation process to determine the values of the six parameters that would provide deformation predictions with the best possible match with the target behaviour recorded at the 44 points. During this process, the cornea and the sclera were allowed to have different material parameters in order to account for the possible variation in fibril size and packing manner – cornea had thinner fibrils uniformly arranged in stromal lamellae while sclera had thicker fibrils arranged less orderly in interwoven bundles (Komai and Ushiki, 1991, Borcherding et al., 1975), Figure 2c.

The process benefitted from the results of earlier shear tests carried out on square 3×3 mm tissue specimens extracted from the central corneas of 12 human donors with ages between 30 and 100 years (Elsheikh et al., 2009). The specimens were subjected to shear stresses caused by two opposite loads applied on the specimen's top and bottom surfaces. Analysis of the results of these tests in our earlier study resulted in values of 0.009MPa, 0.319 MPa and 2.0 for C_{10}, μ_2 and γ_2 , respectively, for corneas over this age range (Whitford et al., 2015). These three inputs meant that the iterative inverse analysis process conducted in this study concentrated on μ_1 and $\gamma_1$for both the cornea and the sclera, and μ_2 and γ_2 for the sclera.

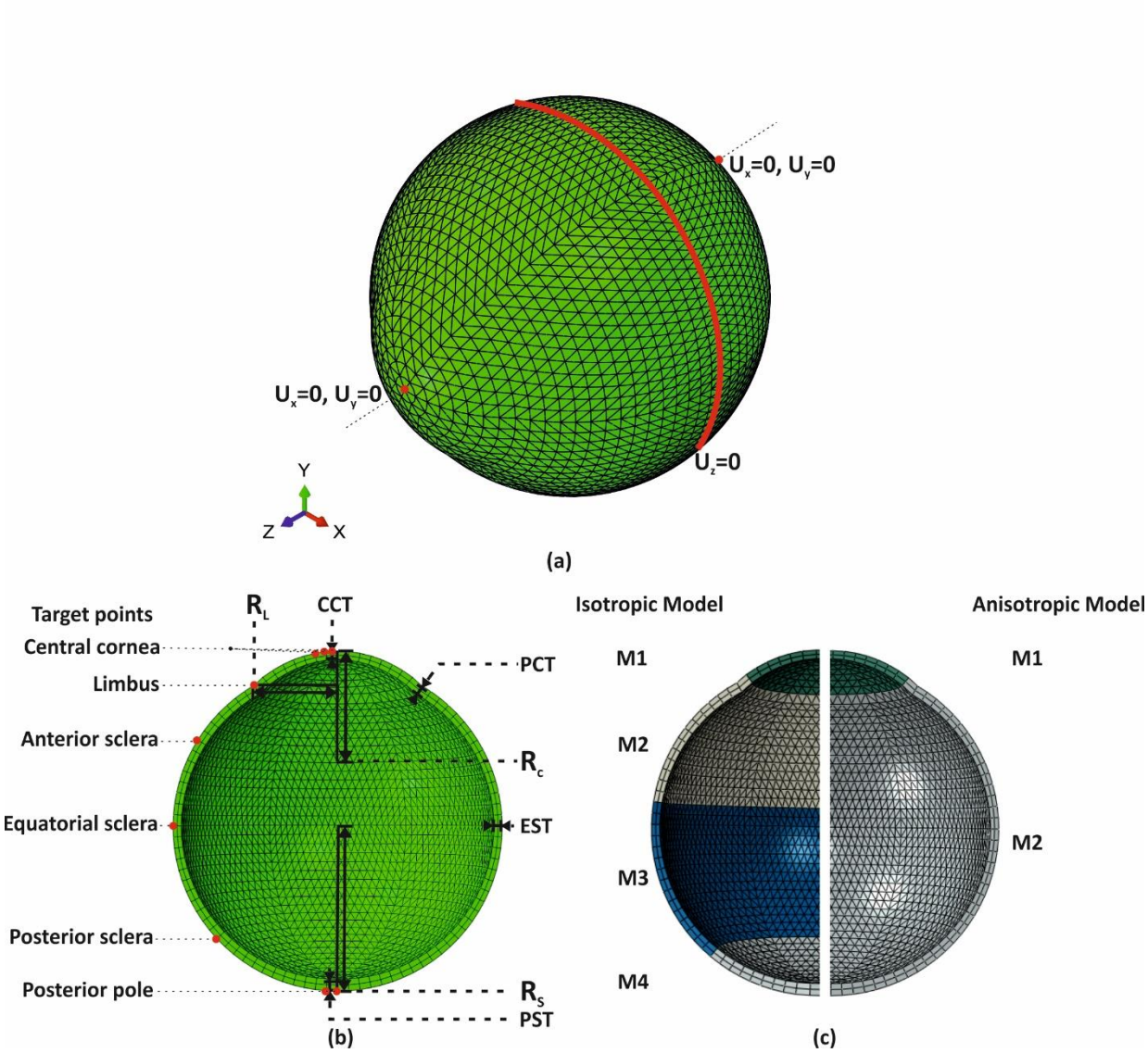

Figure 2 Schematic views of an FE model showing geometry and material sections used in inverse analysis. (a) Constraint conditions illustrated on 3D geometry. (b) Geometric parameters used to create numerical models including R_c, central corneal radius = 7.8 mm (Dubbelman et al., 2002, Dubbelman et al., 2006), CCT, central corneal thickness = 0.545 mm (Avitabile et al., 1997), PCT, peripheral corneal thickness = 0.695 mm, R_L, limbal radius = 5.85 mm (Piñero et al., 2008, Hashemi et al., 2015), R_S, scleral radius = 11.5 mm (Jesus et al., 2017), EST, equatorial thickness = 0.556 mm (Elsheikh et al., 2010a), PST, posterior pole thickness = 0.834 mm and p, corneal shape factor = 0.82; some target points are shown by red dots on one meridian in (b). The ocular model is shown with regions in (c), each has a separate set of Zernike polynomials at each fibril orientation.

Optimisation tool

The Particle Swarm Optimisation (PSO) method was used in the optimisation part of the inverse analysis process. The algorithm was developed by Eberhart and Kennedy (1995) and has been widely applied in engineering applications (Liu et al., 2008, Liu et al., 2007, Mthembu et al., 2011). In this study, the algorithm was implemented in MATLAB (R2018b) in conjunction with the Abaqus FE solver. The iterative analysis was set to be automatically terminated when the root mean square (RMS) of the absolute error (err) in Equation 8, in the pressure-deformation curves between the target performance and the model behaviour became lower than a pre-set threshold of 5% of the maximum displacement of target curves. The absolute RMS error could be expressed as:

$$err = \frac{1}{N_{ld}} \sum_{j_{tc}=1}^{N_{ld}} \left[\sqrt{\frac{\sum_{i=1}^{n_p} (u_i - U_i)}{n_p}} / U_{max} \right]_{j_{tc}} \quad (7)$$

where n_p is the number of points on each pressure-deformation target curve, N_{ld} the number of pressure-deformation plots (31), u_i, U_i the displacement values at each specific pressure in the FE analysis and the target curve, respectively, and U_{max} the displacement under the maximum pressure as obtained from the target curve. The term $\sqrt{\frac{\sum_{i=1}^{n}(u_i - U_i)}{n_p}}$ is the RMS value for each target curve considered and err the average error value. All FE simulation runs were performed on a parallel Linux high performance computing cluster with eight cores and 4000Mb Random Access Memory (RAM) each.

Results

Analysis of Zernike fitting

Zernike polynomials with orders between 5 and 25 were assessed and found to perform differently in the 4 ocular zones. In the central cornea, the fitting error decreased from 22.8±2.4% at order 5 to 2.3±0.18% at order 25, Figure 3a. The overfitting error initially decreased from 19.6±3.2% with order 5 to 18.6±2.4% with order 10, then increased sharply to 3068.9±439.0% at order 25, Figure 3a. In comparison, the limbus, anterior and equatorial sclera, and posterior sclera showed smaller reductions in the fitting error with increased order from 5 to 25 (from 25.1±1.8% to 17.0±1.6%, from 30.7±1.1% to 22.2±0.7%, and from 30.0±1.0% to 18.9±1.1% in the three regions, respectively), Figures 3b, c, d. However, overfitting became significant for the limbus and posterior sclera. The limbus experienced an increase in overfitting error from 24.4±1.6% to 47.3±6.0% with increasing the order from 13 to 25, Figure 3b. On the hand, overfitting increase occurred earlier in the posterior sclera; at order 8 and increased by only 1.5% at order 10 but then kept rising from 28.3±1.6% at order 10 to 36766.0±8941.5% at order 25, Figure 3d. These results pointed at order 10 as being suitable for all 4 zones.

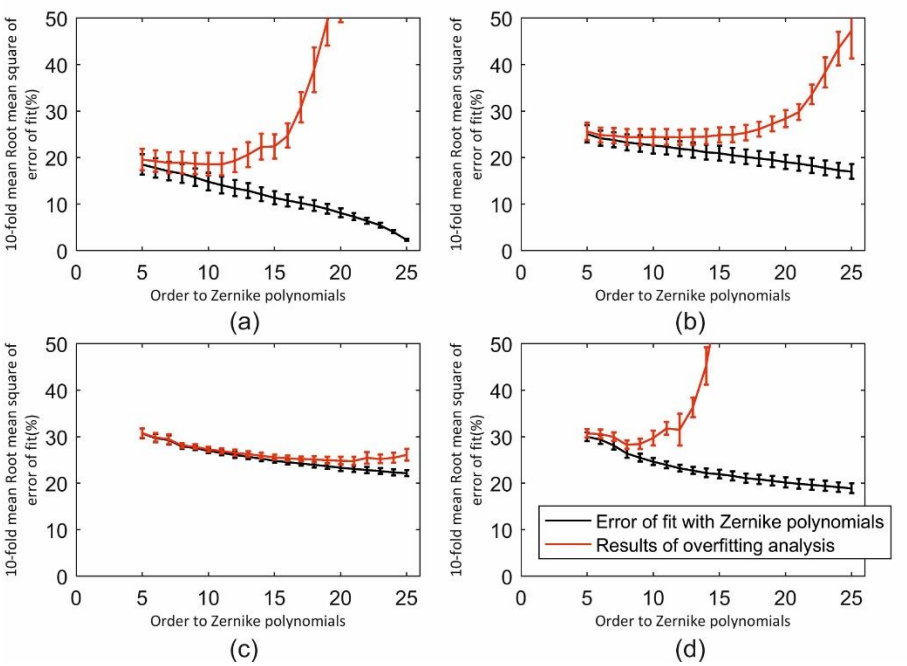

Figure 3 Errors of fit (black line)and overfitting (red line) with Zernike polynomials with orders between 5 and 25 in (a) zone 1: the cornea, (b) zone 2: the limbus, (c) zone 3: the equatorial sclera, and (d) zone 4: the posterior sclera. The mean fitting error relative to the average fibril density was calculated by the ten-fold cross-validation and its standard deviation for 180 orientation.

Optimum number of fibril orientations

Starting from 180 orientations (with an angular step of 1^{o}), in which the raw X-ray scattering data was provided in, a study was carried out to determine the optimum number of orientations that can be used in building numerical models with a reasonable compromise between analysis accuracy and cost (Studer et al., 2010, Pinsky et al., 2005, Whitford et al., 2015). As expected, decreasing the number of orientations led to gradual increases in the model prediction errors, which became exponential when fewer than 16 orientations were adopted, Figure 4. Meanwhile, the analysis cost showed an opposite trend with significant cost reductions with fewer orientations. Based on these results, subsequent work adopted 16 fibril orientations in building ocular numerical models in this study.

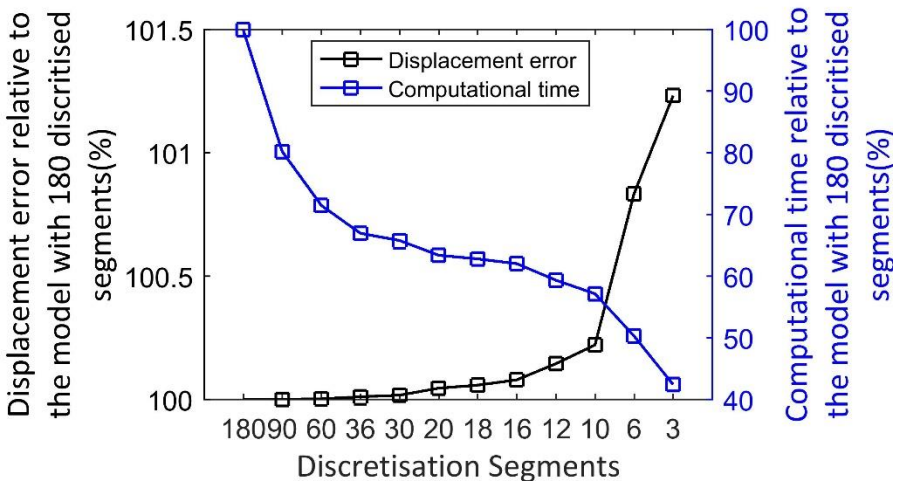

Figure 4 Variations in apical displacement predictions and analysis cost relative to the case with 180 fibril orientations when considering different orientation numbers between 3 and 180

Mesh convergence study

Figure 5 shows that significant reductions in the mesh density of FE models by up to 36% (from 46464 elements to 29400 elements), which led to 47% reductions in numerical analysis cost, caused only an 0.2% change in apical displacement prediction. A further reduction in the number of model elements from 29400 to 12696 caused a change in output by 0.8%, and this increased to 5.0% when the number of elements was cut down from 12696 to 6936. Based on these results, a mesh density with 12696 elements was selected for use in this study.

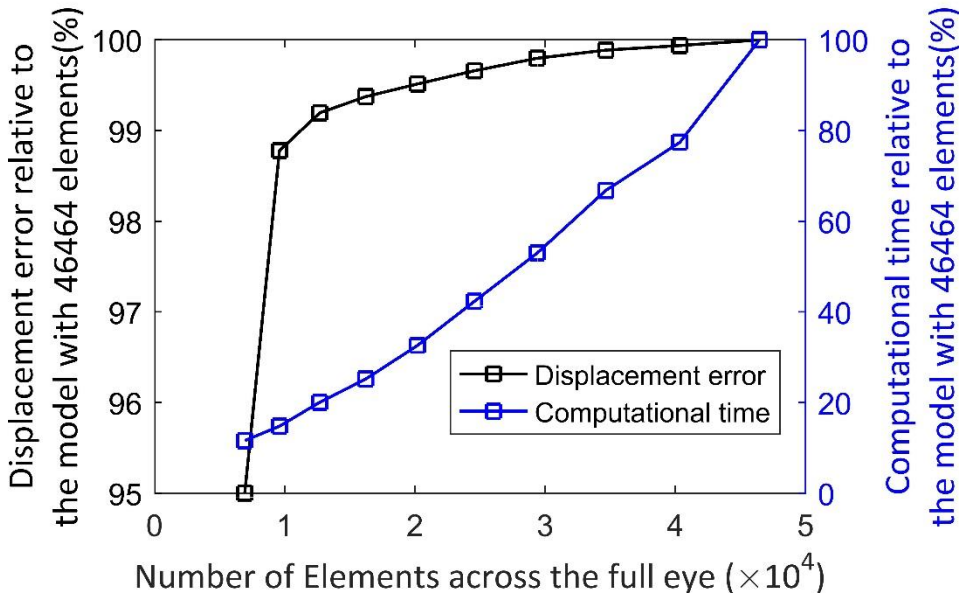

Figure 5 Apical displacement outputs and CPU computation time of numerical models with different mesh densities

Inverse analysis

Inverse analysis was carried out to determine the parameters of the material model that provide the best match for numerical predictions of behaviour with the tissue behaviour obtained in earlier experimental studies in which cornea and sclera specimens (from donors aged between 50 and 90 years) were loaded under inflation conditions while monitoring their deformation (Geraghty et al., 2012, Elsheikh et al., 2010b). The match between the numerical predictions and the experimental measurements was assessed using the particle swarm optimisation (PSO) method, which has been used previously, with success, in solving optimisation problems (Mthembu et al., 2011). The inverse analysis process continued until the RMS of error between predicted and target pressure-deformation behaviour became lower than a pre-set threshold of 5%. At the end of the analysis, the output performance was as presented in Figure 6, with the corresponding values of material parameters included in Table 1. The central cornea exhibited larger axial and lateral displacements, both experimentally and numerically, compared with the sclera and the limbus. Displacements of all regions decreased with age, which was consistent with the expected age-related stiffening (Elsheikh et al., 2007, Geraghty et al., 2012). Of particular note, the material parameters,

produced by the optimisation process, accurately reproduced the experimental displacement curves of the central cornea, limbus and posterior pole.

A uniqueness test was also carried out within the inverse analysis exercise to assess the reliability of the material parameters obtained. Three inverse analysis attempts were conducted with different initial values assigned to the material parameters in the case for tissue with age 50 years. The results, shown in Table 2, illustrated the independence of the inverse analysis output from the initial material parameter values. The results in Table 1 show that the material parameters underwent consistent changes with age with the cornea's μ_1 and γ_1 both undergoing gradual increases. From 50 years old to 90, the value of μ_1 increased from 1.16×10^{-3} to 1.49×10^{-3}, and the value of γ_1 from 121.2 to 134.1. On the other hand, the value of μ_1 increased with age in the sclera from 4.44×10^{-5} at 50 years old to 8.74×10^{-5} at 90, and γ_1 almost remained at the same level in all ages. The increase in the values of parameters μ_1 and γ_1 indicates greater tangent modulus of fibrils on the tangential plane of ocular surface and thus the stiffening of ocular tissue.

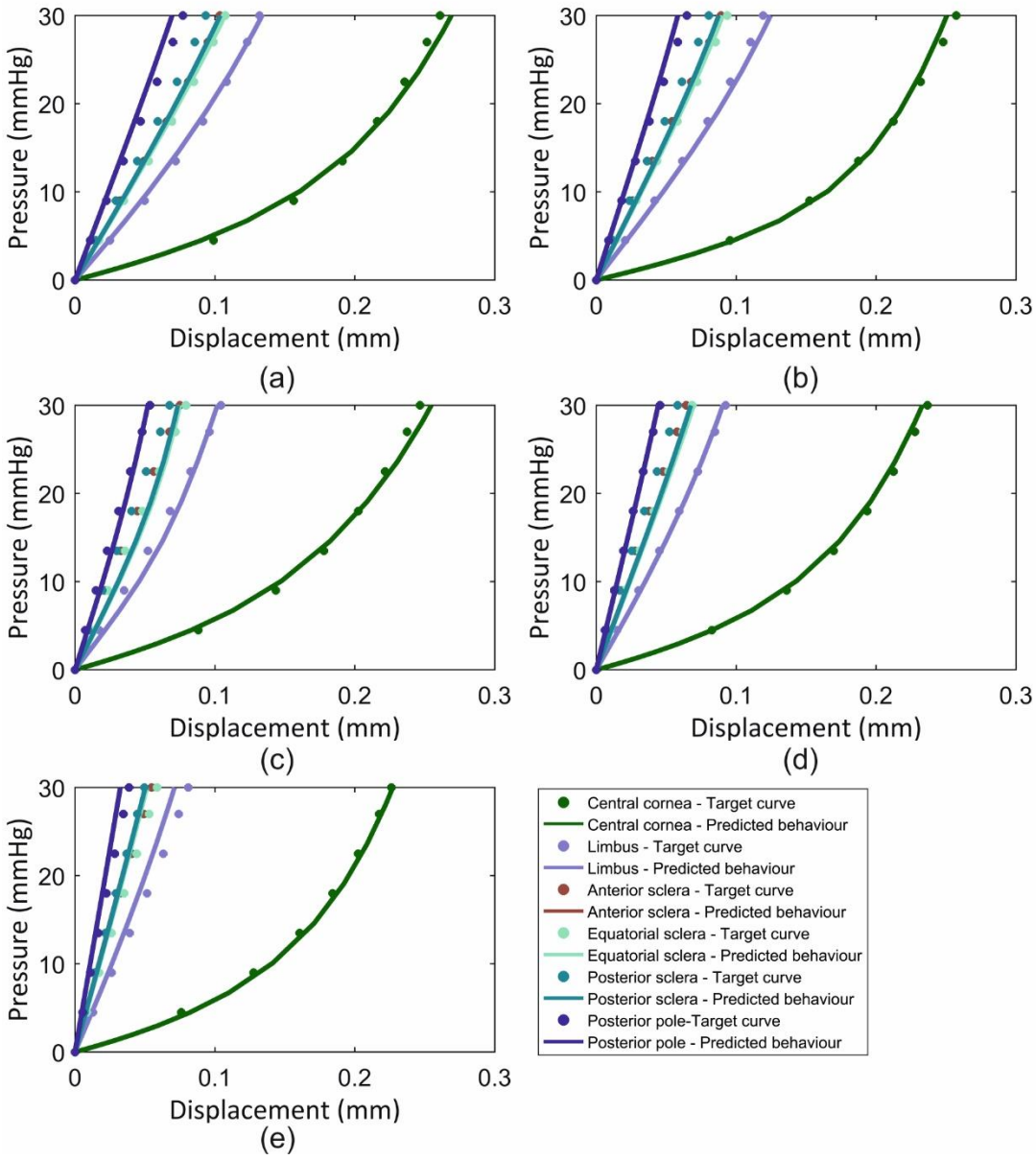

Figure 6 Target curves based on experimental material behaviour obtained for different regions of ocular globe (Figure 2) and for different ages are compared with the predicted behaviour following conclusion of the inverse analysis procedure. (a) to (e) correspond to behaviour of tissue aged 50, 60, 70, 80 and 90 years, respectively.

Table 1 Values of material parameters obtained by inverse analysis for ocular tissues with ages between 50 and 90 years

Age (years)		D	C_{10} (MPa)	μ_1 (MPa)	γ_1	μ_2 (MPa)	γ_2	err (%)
50	Cornea	1×10^{-5}	0.009	1.16×10^{-3}	121.2	*0.319*	*2.0*	3.7
	Sclera			4.44×10^{-5}	532.6	1.48	10.0	
60	Cornea	1×10^{-5}	0.009	1.24×10^{-3}	124.2	*0.319*	*2.0*	4.1
	Sclera			4.90×10^{-5}	535.6	1.68	5.87	
70	Cornea	1×10^{-5}	0.009	1.44×10^{-3}	125.7	*0.319*	*2.0*	4.3
	Sclera			6.02×10^{-5}	535.6	2.7	3.6	
80	Cornea	1×10^{-5}	0.009	1.46×10^{-3}	132.2	*0.319*	*2.0*	3.6
	Sclera			7.52×10^{-5}	524.6	1.48	10.0	
90	Cornea	1×10^{-5}	0.009	1.49×10^{-3}	134.1	*0.319*	*2.0*	3.9
	Sclera			8.74×10^{-5}	536.9	2.43	9.98	

Table 2 Results of a uniqueness test showing material parameters obtained from three inverse analyses using the 50-year-old deformation profile

Inverse analysis	Age (years)		D	C_{10} (MPa)	μ_1 (MPa)	γ_1	μ_2 (MPa)	γ_2	err (%)
1	50	Cornea	1×10^{-5}	0.009	1.16×10^{-3}	121.2	*0.319*	*2.0*	3.7
		Sclera			4.44×10^{-5}	532.6	1.48	10.0	
2	50	Cornea	1×10^{-5}	0.009	1.15×10^{-3}	121.4	*0.319*	*2.0*	3.6
		Sclera			4.45×10^{-5}	532.7	1.22	8.94	
3	50	Cornea	1×10^{-5}	0.009	1.16×10^{-3}	121.6	*0.319*	*2.0*	3.7
		Sclera			4.44×10^{-5}	532.3	1.24	10	

Discussion

In recognition of the collagen fibrils' role as the main load-carrying component in ocular tissue, research has progressed to develop numerical models of ocular mechanical behaviour that rely on microstructural, fibril distribution maps in controlling the distribution of tissue stiffness and anisotropy (Pinsky et al., 2005, Petsche et al., 2012, Pinsky and Datye, 1991, Whitford et al., 2015, Coudrillier et al., 2015, Girard et al., 2009, Pandolfi and Manganiello, 2006, Studer et al., 2010). This study aimed to extend this work in two significant ways; to cover the full ocular globe, instead of limiting coverage to the cornea or the posterior sclera, and to rely on raw, eye-specific X-ray scattering data instead of idealisations of fibril distribution maps. Data at each measurement point, which included fibril content estimates in 180 directions, were grouped into 16 segments to significantly reduce computational time. The data within each of these segments were then fitted to Zernike polynomials to enable the estimate of values of fibril content at the FE integration points, which have different locations from the X-ray measurement points. With the fibril data on content and orientation represented by Zernike polynomials, the constitutive model could rely on this data in reproducing the regional variation of both stiffness and anisotropy. A further exercise was then conducted to use this model, along with the experimentally observed ocular mechanical response to laboratory loading under IOP up to 30 mmHg, to estimate values for the model's material parameters that represent behaviour of tissue aged 50 to 90 years.

This study was built on available corneal microstructure mathematical models and extended the constitutive material model to full-eye application (Whitford et al., 2015, Studer et al., 2010). The X-ray scattering data in the form of fitted Zernike polynomial parameters were used to provide precise fibril distribution at each integration point and to account for the tissue's strong anisotropy. The material model used produced stable behaviour even with reasonable variations in mesh density and during the inverse analysis study.

The iterative inverse analysis procedure provided a distinctive set of material parameters for each of the cornea and sclera. This approach was adopted because of fundamental variations in fibril diameter and arrangement in the two regions. While fibril diameter in the cornea

ranged between 25 and 35 nm, it was between 25 and 230 nm in the sclera (Komai and Ushiki, 1991). Moreover, whereas fibrils were packed in a mainly parallel manner in the cornea, they were more interwoven in the sclera. These variations would affect the material behaviour even with the same collagen content.

The increase of both material parameters μ_1 and γ_1 in the cornea and only μ_1 in the sclera led to reductions in displacement values across the ocular globe with age, Figure 6. The stiffening of the cornea and sclera with age was studied earlier and evidenced through increases in tangent modulus (Geraghty et al., 2012, Elsheikh et al., 2010b). In our study, μ_1 in the cornea increased by 28.5% from 50 years old to 90 while the value of γ_1 increased slightly by 10.6%. The corresponding increase in μ_1 in the sclera was significantly higher; at 96.8%, while γ_1 remained almost constant. The variation in values of parameters μ and γ points at distinctive behaviour differences between the cornea and sclera. While μ controls the initial stiffness, or initial gradient of the stress-strain relationship, γ controls how this initial stiffness varies with further stress. The results show that the cornea had higher initial stiffness of in-plane fibrils but lower rate of stiffness growth than the sclera. For out-of-plane fibrils, the cornea showed both lower initial stiffness and lower rate of stiffness growth than the sclera.

While previous studies adopted 180 discretised orientations for the angular fibril distribution (Whitford et al., 2015, Machyshyn et al., 2010, Studer et al., 2010), this study investigated the effect of reducing number of discretisation segments on numerical model predictions. Having fewer fibril orientations would simplify the process to integrate fibril contribution in the numerical implementation of the strain energy function – reducing the number of Zernike polynomials needed to describe fibril distribution in each orientation, and subsequently simplify the construction of the element stiffness matrices. The optimum number of fibril orientations in our study was 16, at which there was a 0.08% change in numerical model output associated with a 40.0% reduction in analysis cost.

The study has a number of limitations, which should be noted. First, the lack of information on the out-of-plane orientation and density of inter-lamellae fibrils made it necessary to assume an out-of-plane fibril elevation angle of $15°$ and the same angular density distribution as lamellae fibrils, both of which were adopted in an earlier study Studer et al. (2010) and Whitford et al. (2015). This assumption could affect the model behaviour under shear, which would be important in applications subjecting the tissue to flexural effects such as tonometry loading. Second, the material model assumed that the ground substance matrix had the same composition across the whole eye, allowing C_{10} to have the same value in both the cornea and sclera. Future research should explore the validity of this assumption and its effect on ocular behaviour predictions. Third, variations in fibril distribution through tissue thickness were disregarded in model construction as they could not be characterised using X-ray scattering technique. The assumption of uniform fibril distribution across tissue thickness, which was necessary in this study, should be explored in future work while bearing in mind that this will be a challenging, expensive and time-consuming task.

In conclusion, this study presented a constitutive material model that covered the whole eye surface and incorporated the X-ray microstructure characteristics measured for seven ex-vivo human eyes. By considering experimental pressure-deformation behaviour and using an inverse analysis procedure, the model's parameters could be determined to represent tissue behaviour and its age-related stiffening. The current full-eye constitutive model can be used for assessment of clinical challenges including simulation of medical or surgical procedures that interact or interfere mechanically with the eye.

References

AGHAMOHAMMADZADEH, H., NEWTON, R. H. & MEEK, K. M. 2004. X-Ray Scattering Used to Map the Preferred Collagen Orientation in the Human Cornea and Limbus. *Structure,* 12**,** 249-256.

ANDERSON, K., EL-SHEIKH, A. & NEWSON, T. 2004. Application of structural analysis to the mechanical behaviour of the cornea. *Journal of the Royal Society Interface,* 1**,** 3-15.

AVITABILE, T., MARANO, F., UVA, M. G. & REIBALDI, A. 1997. Evaluation of central and peripheral corneal thickness with ultrasound biomicroscopy in normal and keratoconic eyes. *Cornea,* 16**,** 639-644.

BJÓRCK, A. 1996. *Numerical Methods for Least Squares Problems*, Society for Industrial and Applied Mathematics (SIAM, 3600 Market Street, Floor 6, Philadelphia, PA 19104).

BORCHERDING, M. S., BLACIK, L. J., SITTIG, R. A., BIZZELL, J. W., BREEN, M. & WEINSTEIN, H. G. 1975. Proteoglycans and collagen fibre organization in human corneoscleral tissue. *Experimental Eye Research,* 21**,** 59-70.

CARVALHO, L. A. 2005. Accuracy of Zernike Polynomials in Characterizing Optical Aberrations and the Corneal Surface of the Eye. *Investigative Ophthalmology & Visual Science,* 46**,** 1915-1926.

COUDRILLIER, B., PIJANKA, J., JEFFERYS, J., SORENSEN, T., QUIGLEY, H. A., BOOTE, C. & NGUYEN, T. D. 2015. Collagen structure and mechanical properties of the human sclera: analysis for the effects of age. *Journal of biomechanical engineering,* 137**,** 041006.

DUBBELMAN, M., SICAM, V. A. D. P. & VAN DER HEIJDE, G. L. 2006. The shape of the anterior and posterior surface of the aging human cornea. *Vision Research,* 46**,** 993-1001.

DUBBELMAN, M., WEEBER, H. A., VAN DER HEIJDE, R. G. L. & VÖLKER-DIEBEN, H. J. 2002. Radius and asphericity of the posterior corneal surface determined by corrected Scheimpflug photography. *Acta Ophthalmologica Scandinavica,* 80**,** 379-383.

EBERHART, R. & KENNEDY, J. A new optimizer using particle swarm theory. Micro Machine and Human Science, 1995. MHS'95., Proceedings of the Sixth International Symposium on, 1995. IEEE, 39-43.

ELSHEIKH, A., ALHASSO, D. & RAMA, P. 2008a. Biomechanical properties of human and porcine corneas. *Experimental eye research,* 86**,** 783-790.

ELSHEIKH, A., BROWN, M., ALHASSO, D., RAMA, P., CAMPANELLI, M. & GARWAY-HEATH, D. 2008b. Experimental assessment of corneal anisotropy. *Journal of refractive surgery,* 24**,** 178-187.

ELSHEIKH, A., GERAGHTY, B., ALHASSO, D., KNAPPETT, J., CAMPANELLI, M. & RAMA, P. 2010a. Regional variation in the biomechanical properties of the human sclera. *Experimental eye research,* 90**,** 624-633.

ELSHEIKH, A., GERAGHTY, B., RAMA, P., CAMPANELLI, M. & MEEK, K. M. 2010b. Characterization of age-related variation in corneal biomechanical properties. *Journal of the Royal Society Interface***,** rsif20100108.

ELSHEIKH, A., ROSS, S., ALHASSO, D. & RAMA, P. 2009. Numerical study of the effect of corneal layered structure on ocular biomechanics. *Current eye research,* 34**,** 26-35.

ELSHEIKH, A., WANG, D., BROWN, M., RAMA, P., CAMPANELLI, M. & PYE, D. 2007. Assessment of corneal biomechanical properties and their variation with age. *Current eye research,* 32**,** 11-19.

GEFEN, A., SHALOM, R., ELAD, D. & MANDEL, Y. 2009. Biomechanical analysis of the keratoconic cornea. *Journal of the mechanical behavior of biomedical materials,* 2**,** 224-236.

GEISSER, S. 2017. *Predictive inference*, Routledge.

GERAGHTY, B., JONES, S. W., RAMA, P., AKHTAR, R. & ELSHEIKH, A. 2012. Age-related variations in the biomechanical properties of human sclera. *Journal of the mechanical behavior of biomedical materials,* 16**,** 181-191.

GIRARD, M. J. A., DOWNS, J. C., BURGOYNE, C. F. & SUH, J. K. F. 2009. Peripapillary and Posterior Scleral Mechanics—Part I: Development of an Anisotropic Hyperelastic Constitutive Model. *Journal of Biomechanical Engineering,* 131**,** 051011-051011-9.

GRYTZ, R. & MESCHKE, G. 2009. Constitutive modeling of crimped collagen fibrils in soft tissues. *Journal of the Mechanical Behavior of Biomedical Materials,* 2**,** 522-533.

HANNA, K. D., JOUVE, F., BERCOVIER, M. H. & WARING, G. O. 1988. Computer simulation of lamellar keratectomy and laser myopic keratomileusis. *Journal of refractive surgery,* 4**,** 222-231.

HASHEMI, H., KHABAZKHOOB, M., EMAMIAN, M. H., SHARIATI, M., YEKTA, A. & FOTOUHI, A. 2015. White-to-white corneal diameter distribution in an adult population. *Journal of current ophthalmology,* 27**,** 21-24.

JESUS, D. A., KEDZIA, R. & ISKANDER, D. R. 2017. Precise measurement of scleral radius using anterior eye profilometry. *Contact Lens and Anterior Eye,* 40**,** 47-52.

KLING, S. & HAFEZI, F. 2017. Corneal biomechanics–a review. *Ophthalmic and Physiological Optics,* 37**,** 240-252.

KOHAVI, R. A study of cross-validation and bootstrap for accuracy estimation and model selection. Ijcai, 1995. Montreal, Canada, 1137-1145.

KOMAI, Y. & USHIKI, T. 1991. The three-dimensional organization of collagen fibrils in the human cornea and sclera. *Investigative ophthalmology \& visual science,* 32**,** 2244-2258.

LIU, L., LIU, W. & CARTES, D. A. 2008. Particle swarm optimization-based parameter identification applied to permanent magnet synchronous motors. *Engineering Applications of Artificial Intelligence,* 21**,** 1092-1100.

LIU, X., LIU, H. & DUAN, H. 2007. Particle swarm optimization based on dynamic niche technology with applications to conceptual design. *Advances in Engineering Software,* 38**,** 668-676.

MACHYSHYN, I. M., BOVENDEERD, P. H. M., VAN DE VEN, A. A. F., RONGEN, P. M. J. & VAN DE VOSSE, F. N. 2010. A model for arterial adaptation combining microstructural collagen remodeling and 3D tissue growth. *Biomechanics and Modeling in Mechanobiology,* 9**,** 671-687.

MARKERT, B., EHLERS, W. & KARAJAN, N. 2005. A general polyconvex strain-energy function for fiber-reinforced materials. *PAMM,* 5**,** 245-246.

MCDONNELL, P. J. 1996. Constitutive Laws for Biomechanical IVIodeling of Refractive Surgery. *Journal of biomechanical engineering,* 118**,** 473.

MEEK, K. M. & BOOTE, C. 2009. The use of X-ray scattering techniques to quantify the orientation and distribution of collagen in the corneal stroma. *Progress in retinal and eye research,* 28**,** 369-392.

MTHEMBU, L., MARWALA, T., FRISWELL, M. I. & ADHIKARI, S. 2011. Finite element model selection using Particle Swarm Optimization. *Dynamics of Civil Structures, Volume 4***,** 41-52.

NEJAD, T. M., FOSTER, C. & GONGAL, D. 2014. Finite element modelling of cornea mechanics: a review. *Arquivos brasileiros de oftalmologia,* 77**,** 60-65.

PANDOLFI, A. & HOLZAPFEL, G. A. 2008. Three-dimensional modeling and computational analysis of the human cornea considering distributed collagen fibril orientations. *Journal of biomechanical engineering,* 130**,** 061006.

PANDOLFI, A. & MANGANIELLO, F. 2006. A model for the human cornea: constitutive formulation and numerical analysis. *Biomechanics and modeling in mechanobiology,* 5**,** 237-246.

PETSCHE, S. J., CHERNYAK, D., MARTIZ, J., LEVENSTON, M. E. & PINSKY, P. M. 2012. Depth-Dependent Transverse Shear Properties of the Human Corneal Stroma. *Investigative Ophthalmology \& Visual Science,* 53**,** 873-880.

PIJANKA, J. K., ABASS, A., SORENSEN, T., ELSHEIKH, A. & BOOTE, C. 2013. A wide-angle X-ray fibre diffraction method for quantifying collagen orientation across large tissue areas: application to the human eyeball coat. *Journal of Applied Crystallography,* 46**,** 1481-1489.

PIÑERO, D. P., PUCHE, A. B. P. & ALIÓ, J. L. 2008. Corneal diameter measurements by corneal topography and angle-to-angle measurements by optical coherence tomography: evaluation of equivalence. *Journal of Cataract \& Refractive Surgery,* 34**,** 126-131.

PINSKY, P. M. & DATYE, D. V. 1991. A microstructurally-based finite element model of the incised human cornea. *Journal of biomechanics,* 24**,** 907911-909922.

PINSKY, P. M., VAN DER HEIDE, D. & CHERNYAK, D. 2005. Computational modeling of mechanical anisotropy in the cornea and sclera. *Journal of Cataract \& Refractive Surgery,* 31**,** 136-145.

REZAIE, T., CHILD, A., HITCHINGS, R., BRICE, G., MILLER, L., COCA-PRADOS, M., HÉON, E., KRUPIN, T., RITCH, R., KREUTZER, D., CRICK, R. P. & SARFARAZI, M. 2002. Adult-Onset Primary Open-Angle Glaucoma Caused by Mutations in Optineurin. *Science,* 295**,** 1077-1079.

SALIMI, S., PARK, S. S. & FREIHEIT, T. 2011. Dynamic response of intraocular pressure and biomechanical effects of the eye considering fluid-structure interaction. *Journal of biomechanical engineering,* 133**,** 091009.

SIGAL, I. A., FLANAGAN, J. G., TERTINEGG, I. & ETHIER, C. R. 2004. Finite Element Modeling of Optic Nerve Head Biomechanics. *Investigative Ophthalmology \& Visual Science,* 45**,** 4378-4387.

STUDER, H., LARREA, X., RIEDWYL, H. & BUCHLER, P. 2010. Biomechanical model of human cornea based on stromal microstructure. *Journal of Biomechanics,* 43**,** 836-42.

VITO, R. P., SHIN, T. J. & MCCAREY, B. E. 1989. A mechanical model of the cornea: the effects of physiological and surgical factors on radial keratotomy surgery. *Journal of Refractive Surgery,* 5**,** 82-88.

WEISS, J. A., MAKER, B. N. & GOVINDJEE, S. 1996. Finite element implementation of incompressible, transversely isotropic hyperelasticity. *Computer methods in applied mechanics and engineering,* 135**,** 107-128.

WHITFORD, C., MOVCHAN, N. V., STUDER, H. & ELSHEIKH, A. 2017. A viscoelastic anisotropic hyperelastic constitutive model of the human cornea. *Biomechanics and Modeling in Mechanobiology*.

WHITFORD, C., STUDER, H., BOOTE, C., MEEK, K. M. & ELSHEIKH, A. 2015. Biomechanical model of the human cornea: Considering shear stiffness and regional variation of collagen anisotropy and density. *Journal of the Mechanical Behavior of Biomedical Materials,* 42**,** 76-87.

WOLFFSOHN, J. S., SAFEEN, S., SHAH, S. & LAIQUZZAMAN, M. 2012. Changes of corneal biomechanics with keratoconus. *Cornea,* 31**,** 849-854.